Jr.of Industrial Polluction Control 37(7)(2021) pp 1-13
www.icontrolpollluction.com
Research Article

CARBON MONOXIDE CONVERTER EMISSION BY OSMIUM SUPPORT IN ZIRCONIUM DIOXIDE

CARLOS H. DELIZ*

School of Science and Technology, Universidad Ana G Mendez, PO Box 3030, Gurabo PR 00778-3030, Puerto Rico

(Received 22 may, 2021; accepted 06 June, 2021)

Key words: Carbon monoxide, Platinum, Zirconium dioxide, Osmium.

ABSTRACT

The use of zirconia as a catalyst or as a support for metal catalysts has lately become increasingly popular. In recent years, studies of the preparation of doped zirconia producing high thermal stability. Doped zirconia in environmental application is significant to reduce carbon monoxides contribute to several environmental hazards to humans, including respiratory illness, and global warming. One significant drawback to these materials such as platinum and gold is their high cost. Metallic osmium is proposed as a good candidate because it has been shown to be active for CO oxidation and is less expensive than gold and platinum. The osmium electron configuration [Xe] $4f^{14}$ $5d^{6}$ $6s^{2}$ is like platinum electron configuration [Xe] $4f^{14}$ $5d^{9}$ $6s^{1}$.The high orbital d deficiencies causes a stronger interaction with negatively charged molecules. 10% of osmium and platinum were supported on ZrO_2 and prepared by solid by solid, Sol-Gel and Incipient Wetness Impregnation techniques.

INTRODUCTION

Carbon Monoxide (CO), a pollutant that is emitted from many sources. There are numerous applications for which a catalyst capable of oxidizing carbon monoxide to carbon dioxide at low temperatures is desirable (Kermagoret, et al., 2014). Carbon monoxide can form because of incomplete combustion of carbon containing materials. For automotive applications, most of all emissions (80%-90%) are released during the "cold-start" period and materials that have high activity at lower temperatures could help to alleviate pollution from this route (Acres, et al., 2013). Carbon monoxide is one of the major pollutants emitted from vehicular exhausts, industrial off gases, solid fuel combustion and a variety of other sources. Carbon monoxide poisoning occurs both as the result of routine domestic, occupational, and recreational activities, and in the wake of large-scale disasters such as those caused by hurricanes, floods, and winter storms (Avgouropoulos, et al., 2008). A viable route for this air removal is through oxidation to CO_2. For the removal of CO at moderate temperature, it is necessary to catalyze oxidation reaction. Outstanding progress has been made in development of CO oxidation catalysts, and CO emissions have been very effectively controlled from automobiles by using such catalyst technologies (Büchel, et al., 2009). Therefore, low temperature activity, affectivity under high space velocity conditions and chemical stability with lower concentrations of poisonous gases. Research into catalysis is a major field in applied science and involves many areas of chemistry, notably organometallic chemistry, and materials science (Castoldi, et al., 2010).

Catalysis is relevant to many aspects of environmental science, e.g., the catalytic converter in automobiles due high cost and the dynamics of the ozone hole. Catalytic reactions are preferred in environmentally friendly green chemistry due to the reduced amount of waste generated. Many transition metals such as cobalt, platinum and gold were used in heterogeneous catalysis (catalyst differs from the reactants) to reduce pollution emissions, but they are expensive. While the oxidation of carbon monoxide in lean, excess oxygen, conditions have applications for air quality improvement, the preferential oxidation of carbon monoxide in the presence of hydrogen has application for the purification of hydrogen streams for use in fuel cells. Studies showed that an increase in the ratio of CO to O_2 led to higher O_2 selectivity to CO_2 and lower conversion of CO for a given temperature. At a given temperature, the presence of CO_2 or

***Corresponding author's email: cdeliz1@uagm.edu**

H_2O led to an inhibition of the CO oxidation reaction and a decrease in the CO conversion, as compared to the reactions in which CO_2 or H_2O (Chen, et al., 2010). Stability studies showed that operating the catalyst in its oxide form was stable while operating around 100°C, but operation at higher temperatures (175°C-250°C) could lead to a loss of activity, likely caused by the partial reduction of catalytic oxide. At higher temperatures, the reduction of catalytic oxide also led to the formation of methane through the $CO+2H_2$ methanation reaction. Stability studies like cobalt and other catalyst supported on various metal oxide showed that in the test conditions, for example Co/ZrO_2 had the higher activity for the preferential oxidation of carbon monoxide than cobalt on supported on TiO_2, SiO_2, CeO_2, and Al_2O_2 (Daniel, et al., 2010). Some precious metals such as Pt, Pd and Au are well known oxidation catalysts and have received significant attention in emission control catalysis.

One significant drawback to these materials, however, is their high cost. To address this concern, a search for lower cost, alternative materials like has led to the study of transition metal catalysts like metallic osmium (Derrouiche, et al., 2006). The osmium tetra oxide form was excluded as a catalyst because its oxide is toxic. Mechanistic studies for example on CO oxidation in excess O_2 are carried out and transition metal showed cobalt to be an active metal for the reaction, though carbonate formation could lead to decreased activity at temperatures below 100°C (Cant, et al., 2011). Other studies have shown strong promotional effects of CO and Fe to Pt/Al_2O_3 catalysts, leading to substantial activity. Studies without Pt, using other transition metal catalyst indicate that are active for CO oxidation (Chupin, et al., 2006). Data found that the rate of deactivation could be mitigated or eliminated by operating at elevated temperatures or by increasing the ratio of O_2/CO.

MATERIALS AND METHODS

Catalyst Preparation

The catalysts were synthesized by the Incipient Wetness Impregnation (IWI), Sol-Gel (SG) synthesis and solid by solid impregnation technique. The catalyst loadings were denoted by weight percentages. The Incipient Wetness Impregnation technique involves the addition of a solution containing a dissolved metal to a porous catalyst support (Qu, et al., 2006). All the incipient wetness impregnated catalyst in these studies used distilled water as the solvent to dissolve the ZrO2 support (Zirconium oxide MP Lot: R24968) with the active component, metallic osmium (99.9% Acros lot: A0295616) was added/impregnated onto the support. The solution was added drop wise so that then total volume of the solution added to the support. The same procedure was applied to Pt/ZrO_2. (Metallic platinum black 98.0% Acros lot: A03329875) support on (Zirconium oxide MP Lot: R24968). After the impregnation, the catalyst was placed in a drying over at 110°C to evaporate the solvent, leaving the metal on the catalyst support. In some cases, multiple impregnations were used to help reduce possible variations between different particles that could have not been well impregnated. Following the final impregnation step, the catalysts were calcined in air using a ramp rate of 10°C/hour to 300°C then held at the final calcination temperature for at least 3 hours (Gavin, et al., 2014).

The Sol-Gel synthesis method was also employed and can allow additional control of the characteristics of the support and can lead to improved surface area and metal dispersion. Sol-Gel synthesis employs a controlled hydrolysis reaction of a metal alkoxide precursor (Zirconium (IV) isopropoxide) Acros lot: A0321090 with an aqueous solution containing the catalyst's active metal. The synthesis of Sol-Gel catalyst was based on 5 grams of catalyst (Figueroa, et al., 2014). The alkoxide precursor was mixed in a beaker with 50 mL of isopropanol, using a magnetic stir bar. In a separate container, the active metal was dissolved in an aqueous solution and placed in a syringe. To increase the rate of the hydrolysis reaction, the amount of water that was used during the synthesis was greater than the necessary stoichiometric quantity, and a 2:1 ratio of water to metal alkoxide were used (Gates, et al., 2008). The aqueous solution containing the active metal was added to the stirred mixture of isopropanol and the alkoxide precursor at a rate of 0.2 mL/min using a syringe pump. After the aqueous solution had been completed added to the beaker, the gel was left to dry overnight (Qu, et al., 2006). The dried powder was then mixed/crushed using a mortar and pestle and the powder was subsequently calcined in the same manner that was used from the catalyst prepared by Incipient Wetness Impregnation (Hamilton, et al., 2014; Haruta, et al., 2001).

Solid by Solid

The impregnation solid by solid technique involves the addition of metal (osmium or platinum) 10% mixed with porous catalyst support, ZrO_2. 10%=0.5 grams metal/5 grams ZrO_2. The final impregnation step, the catalysts were calcined for at least 3 hours at 300°C. The dried powder was then mixed/crushed using a mortar and mechanic catalytic mixer (Lindholm, et al., 2008; Iglesias, et al., 2010).

Incipient Wetness Impregnation

The impregnation Incipient Wetness Impregnation (IWI) technique involves the addition of osmium or platinum solution 10% (0.5 grams) in water (50 mL) mixed with 5 grams of porous catalyst support such as ZrO_2. The solution was added drop wise in excess (water) to cover all pore volume of the support. Catalyst was placed in a drying over at 110°C to evaporate the water. Catalyst was calcination with ramp rate of 10°C/hour to 300°C.

Sol-Gel Synthesis

Sol-Gel synthesis employs a controlled hydrolysis reaction of a metal alkoxide precursor with an aqueous

solution containing the catalyst's active metal.

Zirconium (IV) propoxide 70% in propanol.

The solution containing the active metal with water, 5 mL is added to the stirred mixture the alkoxide precursor at a rate of 0.2 mL/min using a syringe pump. Note: Additional 5 mL of water to increase the rate of the hydrolysis. 2:1 ratio, 0.500 g metal/5 mL water=0.10 g/mL. Density Zirconium (IV) propoxide is 0.960 g/mL. 5.20 mL (0.96 g/mL)=5 g Zirconium (IV) propoxide. (0.10/0.960) x 100%=10%.

Laboratory micro scale reaction experiments were performed on the reactor system depicted in Fig. 1. The system was equipped with flow controller (ADM1000 Intelligent Flow meter JW) and allowed a wide range of gas velocities to be introduced to the reactor. The reaction temperature was controlled by Lindberg Blue M Thermo Scientific oven and temperature K-type thermocouple linked model Fluke, designed to run at temperatures up to maximum of 700°C and below. The reactors were constructed from ¼ external diameter stainless steel and copper tubing. The catalyst samples were held in cylindrical reactor of 50 mm high x 4.6 mm diameter (Forzatti, et al., 2008). Equilibrium composition of CO oxidation was a highly exothermic reaction and was quite temperature sensitive, So the thermocouple was positioned so it touched the downstream end of the catalyst bed, this ensured an accurate temperature reading that accounts for the heat produced in the reaction (Hao, et al., 2009). Screening experiments were compared catalysts based on equal weights as platinum black support on titanium oxide. The temperature range for testing covered the range of 25°C to 200°C. Reactant concentrations were varied. A variety of analytical equipment was used to monitor the feed and product gas stream compositions. A Bacharach Fyrite Tech Infrared Analyzer CO_2 provided simultaneous and continuous monitoring of CO and CO_2 concentrations (Hongjuan, et al., 2015; Ingelsten, et al., 2005). In addition, GC 5890 HP gaschromatograph equipped with a Thermal Conductivity Detector (TCD) and 5A molecular sieve column as well as phenomenex column (Wachs, et al., 2007). The catalyst was pre–treated in helium flow at 200°C for a period of 30 min to remove any volatile contaminant and adsorbed gases.

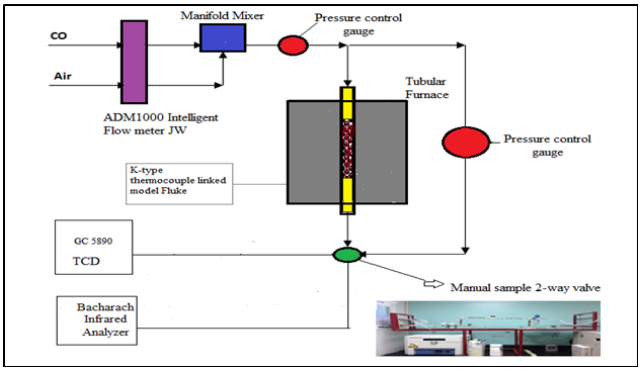

Fig. 1 The experimental oxidation setup.

Material Characterization

Raman spectroscopy: Raman spectra were obtained on powdered samples at room temperature using a Raman Renisaw model 2100 spectrometer with a 10-x microprobe in the back scattering geometry and a 785 nm argon ion laser.

X-ray diffraction (XRD): X-ray Diffractometer, D8 Advance type (Bruker-AXS). Vertical theta-theta goniometer in powder XRD setting; lowest step size (2-θ), with horizontal sample carrier; nine position multiple stage with automatic sample changer; fixed slit system. One dimensional detector (Lynx Eye type) with collection rate about two orders of magnitude. Copper tart X-ray tube used with nickel filter.

SEM jsm-6010la: SEM with resolution 4 nm at 20 kV. Magnification: 5x to 300,000x. Specimen Size: Up to 150 mm diameter and a stage type Eccentric goniometer. On imaging mode with high vacuum: SE (Secondary Electron) and BSE (Back Scatter Electron).

Infrared spectra: The infrared spectra were obtained using FT-IR Nicole Protégé Model 4700 Thermo Electron. The spectrometer lets you collect spectra in the mid-IR, far-IR and near-IR spectral range.

Ultraviolet/Visible scanning spectra: Evolution 201 UV-Visible Spectrophotometer pathway in double–bean with sample and reference cuvette position; Czerny-Turner Monochromator. Spectral Bandwidth (s) 1.0 mm. Operating range 190-1100 nm.

BET: Micromeritics TriStar II 3020, a fully automated, three-station surface area and porosity analyzer with a Krypton Option can extend surface area measurements to as low as 0.001 m^2/g.

TGA: TGA Q50 operating range 50 to 1000°C at 20°C/min using empty platinum pans.

RESULTS AND DISCUSSION

XRD

During the calcinations of the catalysts, in-situ XRD was performed to examine changes and characterization in both Os and Pt support crystal structure. The diffraction patterns during these experiments for the 10% Os catalysts on ZrO_2 and 10% Pt catalyst on ZrO_2 like a referent standard, prepared via solid by solid, IWI and Sol-Gel, were shown in Figs. 2 and 3 respectively. The 10% Os/ZrO_2 and 10% Pt/ZrO_2 IWI catalyst, showed as cubic crystalline form and small amount tetragonal morphology structure of ZrO_2 up until 300°C, diffraction lines at 2-θ values of 18.0°C, 20.0C°, 25.0°C, 28.0°C and 37.0°C for Os/ZrO_2, and 28.0°C, 32.0°C, 40.0°C, 47.0°C and 67.0°C for 10% Pt/ZrO_2, respectively (Forzatti, et al., 2008; Hao, et al., 2009). A narrowing of these peaks indicates the development of increased crystallinity. The diffraction patterns in Figs. 2 and 3 for 10% Os/ZrO_2 and 10% Pt/ZrO_2 Sol-Gel shows different transformation behavior than the catalyst prepared by IWI or solid

by solid. At 300°C, Sol-Gel reaction low crystalline phases were observed, but broad peaks associated with tetragonal form of the ZrO_2 appeared at, the sharpening of the tetragonal form ZrO_2 peaks

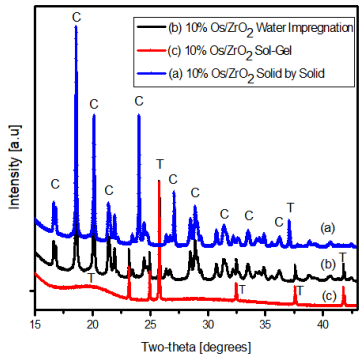

Fig. 2 The diffraction patterns in 10% Os/ZrO_2.

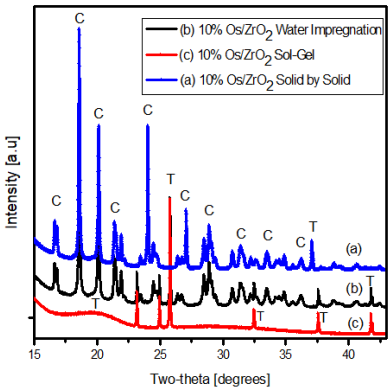

Fig. 3 The diffraction patterns in 10%Pt/TiO_2.

(Kohyama, et al., 2015; Haruta, et al., 1993). The diffraction lines from tetragonal ZrO_2 appear and grow with increasing 2-θ. The diffraction well describes as cubic crystalline phase, although it contains a small amount of tetragonal impurity. Crystalline Os or Pt-oxide phases were detected slightly through XRD in either the Sol-Gel or the IWI preparation.

Laser Raman Spectroscopy

Raman spectra were obtained on powdered samples at room temperature using a Raman Renisaw model 2100 spectrometer with a 10-x microprobe in the back scattering geometry and a 785 nm argon ion laser (Ozbek, et al., 2014). Figs. 4 and 5 show the laser Raman spectra taken over the impregnated solid by solid, Sol-Gel and IWI of the 10% Os/ZrO_2 and 10% Pt/ZrO_2 catalysts at 300°C, respectively. The ZrO_2 bands at 182, 388, 195, 380 cm^{-1} are typical tetragonal form and 1516, 1607, 1535, 1610 cm^{-1} are typical of cubic form of the ZrO_2. For the 10% Os/ZrO_2 and 10% Pt/ZrO_2 catalysts, the ZrO_2 bands were visible (Wang, et al., 2011; Pérez, et al., 2005). The broadening of the ZrO_2 bands may be attributed to interactions with Os and Pt species and disorder in the oxygen sub-lattice (Rivallan, et al., 2009). The lack of metallic osmium raman bands at lower calcinations temperatures on the ZrO_2 supported samples suggests that Os does not form as readily on the surface as compared to the ZrO_2 support. This difference in surface Os was likely related to the differences in CO oxidation activity observed over the ZrO_2 catalysts. These results indicate that osmium and platinum were presents in the 10% Os/ZrO_2 and 10% Pt/ZrO_2 catalyst (Rivera, et al., 1993; Rodriguez, et al., 2013). The lack of clearly visible vibrational bands from the ZrO_2 support in the sample Os/ZrO_2 can was explained by the smaller Raman cross-section of cubic and tetragonal forms of ZrO_2.

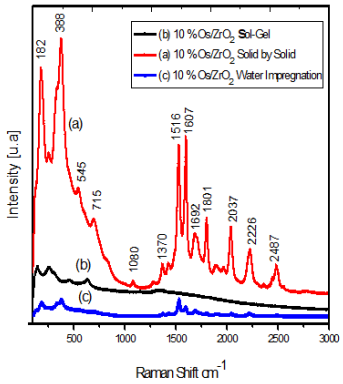

Fig. 4 Laser raman spectroscopy taken over the impregnated solid by solid, Sol-Gel and IWI of 10%Os/ZrO_2.

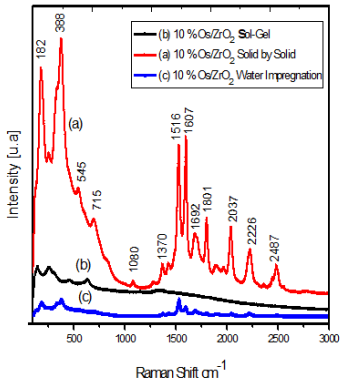

Fig. 5 Laser raman spectroscopy taken over the impregnated solid by solid, Sol-Gel and IWI of 10%Pt/ZrO_2.

FT-IR

The adsorption spectra of the 10% Os/ZrO_2 and 10% Pt/ZrO_2 were obtained to examine the types of surface species using a FT-IR Nicole Protégé Model 470 (Wade, et al., 2006). For 10% Os/ZrO_2 Sol-Gel impregnation, the high wave number region in Fig. 6 exhibits bands at 3500 cm-1 that correspond to terminal, bi-bridged, and tri-bridged OH groups, typical of the OH vibration of physically adsorbed H_2O. For Sol-Gel, IWI and solid by solid were observed by a combination band at 2900 cm^{-1} and the C-H stretch at 2800 cm^{-1}. In the low wave number region, Figs. 6 and 7 were observed from the band at 1484 cm^{-1} as well as the C-H bending and symmetric C-O stretching modes at 1379 cm^{-1} at 1358 cm^{-1}, respectively (Zou, et al., 2010; Xianyong, et al., 2010). Other bands in the 1000-500 cm^{-1} have been assigned to ionic carbonate at 1484 cm^{-1} which shifts to 1440 cm^{-1} and carbonate species at 1300 cm^{-1} and 700 cm^{-1} (Daniel, et al., 2010).

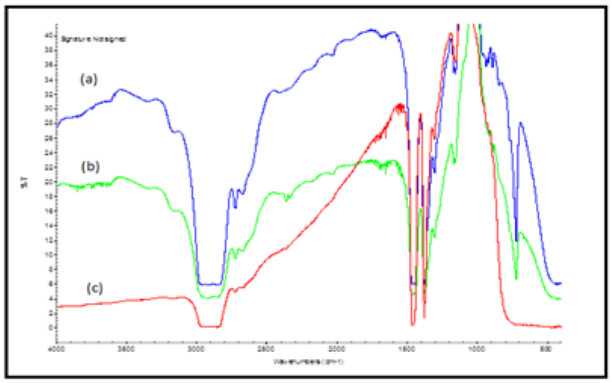

Fig. 6 The adsorption spectra of the 10%Os/ZrO_2.
(a) Os/ZrO_2, Sol-Gel Impregnation
(b) Os/ZrO_2, Incipient wetness impregnation
(c) Os/ZrO_2, Solid by Solid Impregnation

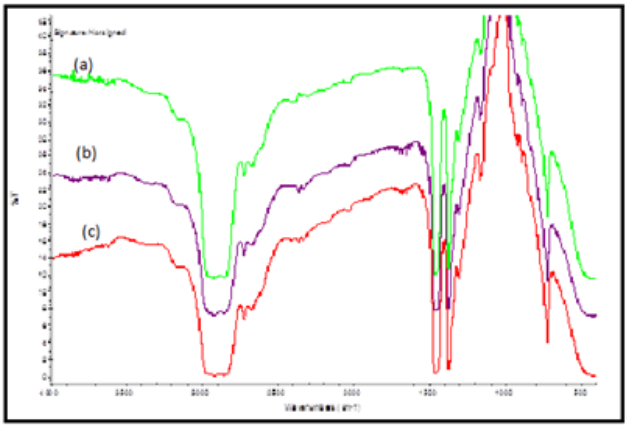

Fig. 7 The adsorption spectra of the 10%Pt/ZrO_2.
(a) Pt/ZrO_2, Sol-Gel Impregnation
(b) Pt/ZrO_2, Incipient wetness impregnation
(c) Pt/$ZriO_2$, Solid by Solid Impregnation

Ultraviolet/Visible Scanning Spectra

Ultraviolet/Visible scanning spectra were obtained on powdered samples at room temperature using a Spectrophotometer Evolution 201 Thermo Scientific. The reading was 600 nm to 200 nm see Fig. 8 and Fig. 9 show the spectra taken over the impregnated solid by solid, Sol-Gel and IWI of the 10% Os/ZrO_2 and 10% Pt/ZrO_2 catalysts at 300°C, respectively, along with reference spectra taken over unloaded (Wonyong, et al., 2014). The fundamental absorption of ZrO_2 appeared in the UV region about 333, 347 nm for Os/ZrO_2 and 382 nm for 10% Pt/ZrO_2. This indicated that UV-Vis absorption was closely related to doping metal ion (Wachs, et al., 2007). The cubic and tetragonal forms were present with high activity in 333 and 382 nm, but we notice that transformation factor in the three different preparation. The dopant element was significant in solid by solid and sol gel preparations with mayor absorbencies. These results show that was concurrent with high catalyst activities (Yasuo, et al., 2009; Young, et al., 2007).

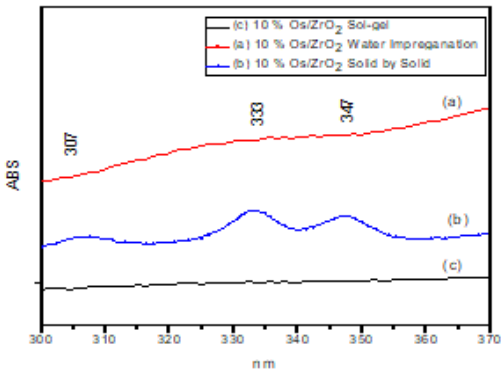

Fig. 8 The spectra taken over the impregnated solid by solid, Sol-Gel and IWI of the 10%Os/ZrO_2.

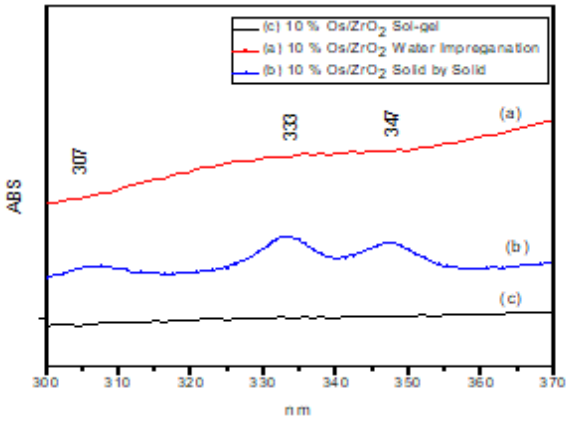

Fig. 9 The spectra taken over the impregnated solid by solid, Sol-Gel and IWI of the 10%Pt/ZrO_2.

BET Surface Area for Catalysts

Surface area analysis was performed over supported metallic osmium catalysts 10%Os/ZrO_2, using BET method with a Micromeritics TriStar II 3020 instrument. N_2 was selected as the adsorbent, and analysis was performed at liquid nitrogen temperature (77 K). The samples were degassed before surface area measurement (Liu, et al., 2014). The results from these experiments were shown in Table 1 (Cheng, et al., 2014; Zhang, et al., 2014). The 10%Os/ZrO_2 catalyst had a significantly lower surface area than the other literature supports. Generally, surface area decreases because of pore blocking/clogging due metallic bond formation (Collins, et al., 2014). If there are not have such effect, either because your pores are too wide or because they are only a low amount of them, then the addition of a new phase at the surface of a substrate should logically create heterogeneity, roughness, and therefore a higher surface area, provided that very small particles were deposited (Yang, et al., 2014; Widmann, et al., 2014; He, et al., 2014; Zhao, et al., 2009; Petoud, et al., 2011). The high catalyst active due to significantly lower micropore volume (Kermagoret, et al., 2014). The catalyst process in gas states were influenced by physiochemical variable such as particular size. The influence of particle size of zirconium on catalytic activities has been

demonstrated. Rivera et el. reported increasing rate of catalyst for zirconium particle in the range of 4-50 nm, photocatalytic and gas catalytic activity increased with decreasing size. The micropore size permitted mayor radio material interaction in adsorption phenomenon versus macropores with minor radio interaction in gas catalyst (Hafizovic, et al., 2007). The micropores exhibit outstanding CO capture and conversion performance at atmospheric pressure and room temperature. As pressure increases, the gas condenses first in the pores with the smallest dimensions. By extending this process so that the gas could condense in the pores, the sample's fine pore structure (Young, et al., 2007; Liu, et al., 2014). The pressure was increased until saturation was reached, at which time all pores are filled with liquid. The adsorptive gas pressure then was reduced incrementally, evaporating the condensed gas from the system. Evaluation of the adsorption and desorption branches of these isotherms and the hysteresis between them reveals information about the size, volume, and area (Rivera, et al., 1993). Chemisorption interaction of an active gas and a solid surface, involving the sharing of electrons between the adsorptive molecule and the solid surface. It was generally assumed that a chemisorbed layer will not exceed a single molecule in thickness. The efficiency of a catalyst in promoting a chemical reaction was related directly to the density of active sites on its surface. In addition, hydrogen reduction of platinum group metal black at elevated temperature can result in a substantial loss of surface area. Thus, an osmium or platinum black heated at 300°C in hydrogen a decline in surface area due to sintering. The reduction on dispersion explains that actives hydrogen proton gain electron particles. This is explaining the possibility that osmium in zirconium oxide could work to generate hydrogen (Kermagoret, et al., 2014).

SEM

Figs.10-15 shows the cross sectional image was obtained on powdered samples at room temperature using a JOEL (JSM-6010LA SEM). The 10% Os/ZrO_2 and 10% Pt/ZrO_2 calcined at 300°C. These micrographs show different particle size distribution with grain size 2 µm to 5 µm (Tsao, et al., 2007; White, et al., 2009). The films were nanoparticles structures that have a microporo size area and help to enhance its sensitivity (Liu, et al., 2015). The particles exhibit a highly ordered morphology. The Energy Dispersive Spectrometer (EDS) was employed to test the average estimation composition of osmium and platinum in zirconium dioxide impregnation, where the main elements were the following results showed in Table 2. The 10% of the precious metal (osmium and platinum) were proportional to 3-10 grams of this metal in automobile catalytic converter (Ning, et al., 2017; Lonergan, et al., 2011).

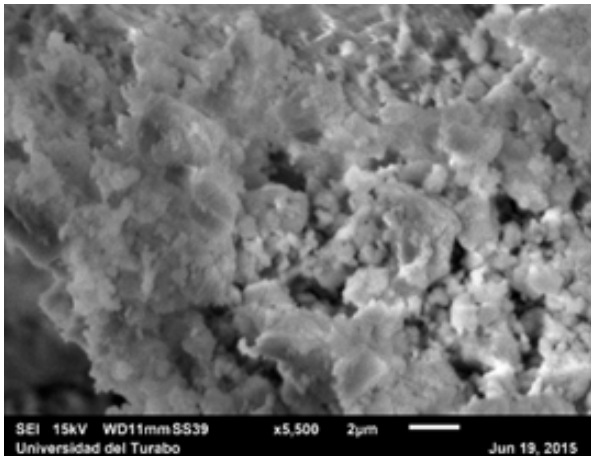

Fig. 10 Morphology of the synthesized samples, incipient wetness impregnation of 10%Os/ZrO_2.

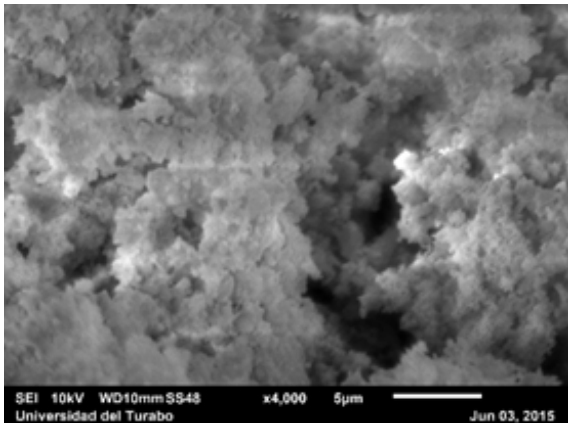

Fig. 11 Morphology of the synthesized samples, incipient wetness impregnation of 10%Pt/ZrO_2.

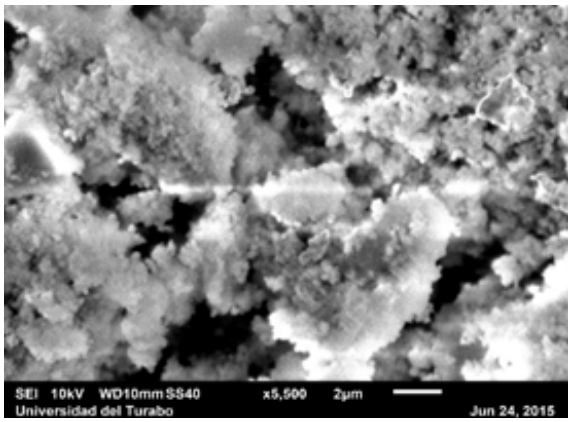

Fig. 12 Morphology of the synthesized samples, Sol-Gel of 10%Os/ZrO_2.

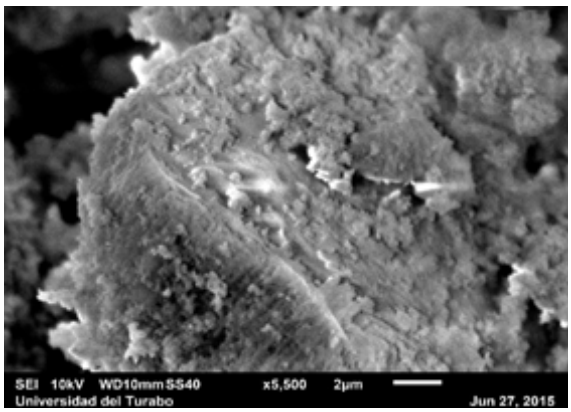

Fig. 13 Morphology of the synthesized samples, Sol-Gel of 10%Pt/ZrO_2.

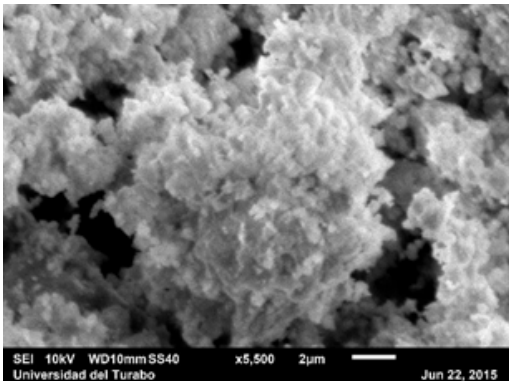

Fig. 14 Morphology of the synthesized samples, solid by solid of 10%Os/ZrO_2.

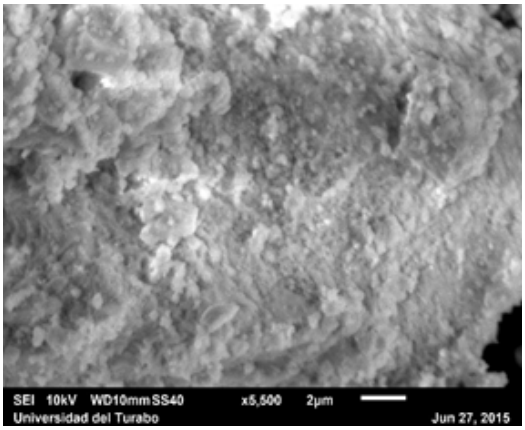

Fig. 15 Morphology of the synthesized samples, solid by solid of 10%Pt/ZrO_2.

Table 1. The samples were degassed before surface area measurement.

Horizons	Synthesis technique	Surface area (m^2/g)	Micropore volume (cm^3/g)	Micropore Area (m^2/g)
10% Os/ZrO_2	Water Imp	2.1615	0.000015	0.0821
10% Os/ZrO_2	Sol-Gel	12.8839	0.002338	5.0029
10% Os/ZrO_2	Solid by Solid	2.2638	0.000010	0.1046

Table 2. Average estimation composition of osmium and platinum in zirconium dioxide impregnation.

	Synthesis technique	ZrO_2 wt%	Oxygen wt%	Metal wt%
10% Os/ZrO_2	Water Imp	71.89%	19.40%	8.71%
10% Os/ZrO_2	Sol-Gel	54.70%	25.37%	19.93%
10% Os/ZrO_2	Solid by Solid	72.60%	18.88%	8.52%
10% Pt/ZrO_2	Water Imp	54.73%	33.54%	11.73%
10% Pt/ZrO_2	Sol-Gel	68.85%	12.52%	18.63%
10% Pt/ZrO_2	Solid by Solid	61.64%	24.37%	13.99%

Thermogravimetry Measurement

The TG curve can be divided into three stages. The first stage Fig. 16 is from room temperature to 300°C, over which the mass loss was the greatest. A mass loss of up 14% was observed, which was caused by dehydration and evaporation of alcohol from the xerogels ((Munir, et al., 2018). The second stage Fig. 17 was from 300°C to 450°C, where the mass loss is 17%. This can be assigned to the combustion and carbonization of most organic contents in the xerogel (Gavin, et al., 2014). The third stage Fig. 18 was from 450°C to 700°C, where the mass loss is about 21%. This is attributed to the oxidation of carbon residue and evaporation of chemisorbed water (Gao, et al., 2017).

Activation Energy

The Arrhenius plot shown in Fig. 19, the activation energy for oxidation of CO to CO_2 over 10% Os/ZrO_2 and 10%Pt/ZrO_2 were calculated in Table 2 (Cheng, et al., 2018). The Sol-Gel technique in both platinum and osmium preparation require less activation energy, so the reactions occur faster (Kasipandi, et al., 2019). The Arrhenius plot was obtained by plotting the logarithm of the rate constant, k, versus the inverse temperature, 1/T. k=Ae-Ea/RT where k represents the rate constant, Ea is the activation energy, r is the gas constant (8.3145 J/K), and T is the temperature expressed in Kelvin. A is known as the frequency factor, having units of L/mol.s. We can graphically determine the activation energy by manipulating the Arrhenius equations to put it into the form of a straight line. Taking the natural logarithm of both sides give us; lnk=-Ea/RT+lnA (Chung, et al., 2019). A slight rearrangement of this equation then gives us a straight-line plot for ln k versus 1/T, where the slope is -Ea/R. ln k (rate constant) data were obtained knowing gas flow velocities (45 mL/minutes) and reactor volume. The value obtained was multiplied by the percentage obtained at the temperature required to complete the entire conversion of CO to CO_2.

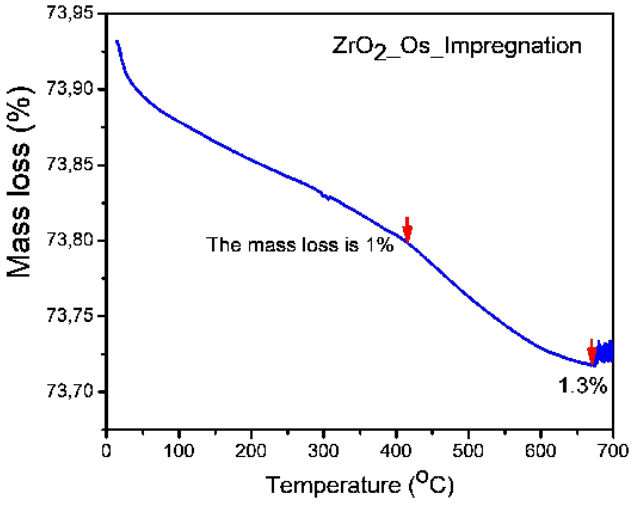

Fig. 16 First stage.

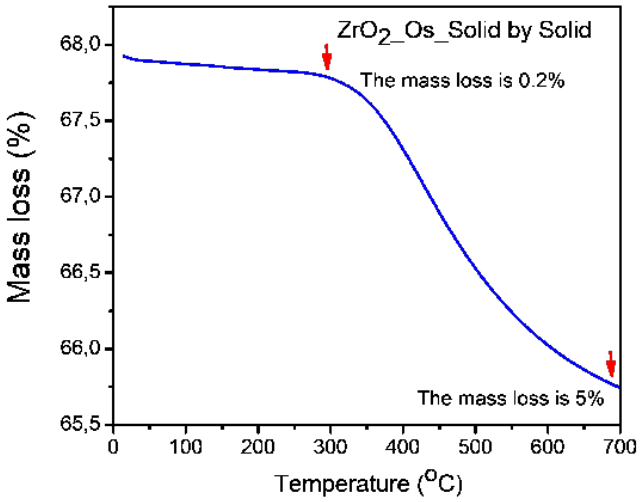

Fig. 17 Second stage.

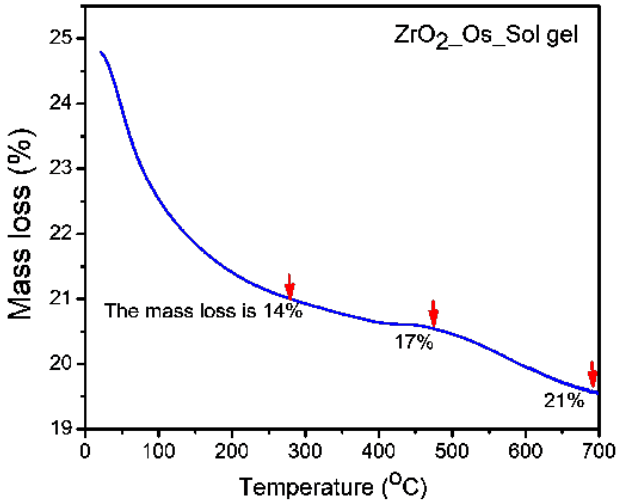

Fig. 18 Third stage.

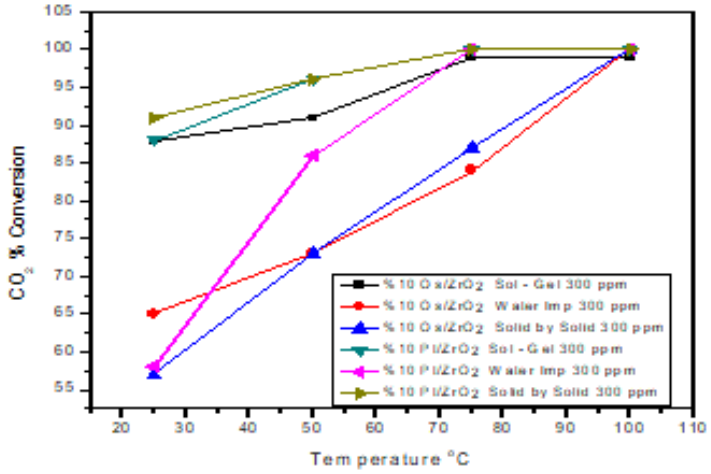

Fig. 19 Arrhenius plot.

CO to CO_2% Conversion, Activity Measurements

The catalytic activity was in terms of % conversion. (X) of CO gas to CO_2 according to the following equation: X CO=(ppm CO in–ppm CO_2 out)/ppm CO in x 100. Time on stream studies at room temperature (25°C) were conducted on the 10% Os/ZrO_2 catalyst using feed streams containing 300 ppm CO (Industrial Scientific) lot # 1500206 in balance with air. Fig. 20 shows the concentrations of CO and CO_2 during the experiment using a feed stream of 45 mL/min. Complete conversion of CO to CO_2 was obtained and no decline in conversion was observed over the course of this experiment (Lonergan, et al., 2011). To further study the catalyst's activity, an additional experiment was conducted using Pt/ZrO_2 standard catalyst under same conditions. During this experiment, the temperature was increased by temperature increments of 25°C. The higher CO concentration in the experiment required elevated temperatures in order to achieve complete conversion of CO to CO_2, which was obtained at 75°C Sol-Gel, waters impregnation and solid by solid impregnation with 10% Pt/ZrO_2 referent standard (Oenema, et al., 2020). The other way with 10% Os/ZrO_2 was obtained at 75°C Sol-Gel technique. The IWI, the completed conversion to 10% Os/ZrO_2 was 100°C and 10% Pt/ZrO_2 was 75°C. The experiment was run over the course of several days and the catalyst was shown to be stable during the course of the experiment, with no decline in activity at any of their ported temperatures. It can be observed in Sol-Gel impregnation to both catalysts that the decrease in CO concentration was accompanied by the simultaneous and fast increase in CO_2 concentration (Sautel, et al., 2000; Gao, et al., 2017). However, water impregnation in 10% Os/ZrO_2, there appeared to be some inhibition effect, with temperature required for complete CO conversion shifting by about 50°C. Water impregnation in Fig. 17 shows that complete conversion of CO was not obtained until about 100°C to 10% Os/ZrO_2 and 100°C to 10% Os/ZrO_2 in solid by solid, possibly due to a competitive adsorption effect (Tsao, et al., 2007). Osmium based catalysts was synthesize and studied both for the low temperature oxidation of CO in low oxygen as well as for the preferential oxidation of CO were found that high activity could be achieved even at room temperature (Hao, et al., 2009; Hongjuan, et al., 2015; Ingelsten, et al., 2005). The reaction studies examined the effect of water, which was found to have an inhibitory effect on CO oxidation.

CONCLUSION

High increasing demand of catalysts for industrial and environmental applications, it is of prime importance to search for improved supports for a variety of reactions. The high activity of catalyst is also of prime importance, which effectively reduces the amount of expensive catalyst. Considering the increasing cost of noble metal-based catalysts for environmental applications, as well as their limited availability, it is of most importance to develop new catalysts with improved catalytic activity under the conditions of practical relevance. This is of interest for industrial CO control; the carbon monoxide can form because of incomplete combustion of carbon-containing materials. For automotive applications, most of all emissions (80%-90%) are released during the "cold-start" period and materials that have high activity at lower temperatures could help to alleviate pollution from this route. 100% CO to CO_2 conversion was observed in a temperature range 75°C to 100°C, on space velocity 3250 h^{-1} micro scale reactor and initial CO concentrations at 300 ppm. For the oxidation catalysts, osmium supported on ZrO_2 was shown to have high activity. The Arrhenius plot showed the activation energy for oxidation of CO to CO_2 over 10% Os/ZrO_2 and 10% Pt/ZrO_2. The Sol-Gel technique in both platinum and osmium preparation require less activation energy, so the reactions occur faster. The loss alcohols allow in Sol-Gel impregnation the exothermic tetragonal phase transition to cubic phase to occur Sol-Gel and solid by solid synthesis techniques were examined, with overall higher activity. Studies using SEM, XRD, FT-IR, UV, BET and Raman spectroscopy were consistent with this observation and its characterization; however, in activity measurements platinum was more oxidized in ZrO_2. Osmium could be alternative material. Osmium was proposed as a good candidate because it has been shown to be active for CO oxidation and is less expensive than gold and platinum. Concluded that the presence of osmium and the support's ability to promote the formation of CO_2. The oxidation of CO was complete over most of the temperature range, indicating that the osmium mixed catalyst bed can work to eliminate CO.

REFERENCES

Kermagoret A, Nathaniel KR, Matthew PC and Emmanuel C. 2014. Chlorodiethylaluminum supported on silica: A dinuclear aluminum surface species with bridging M_2-Cl-ligand as a highly efficient co-catalyst for the Ni-catalyzed dimerization of ethene. *J Catal*. 313:46.

Acres K and Swart K. 2013. Gmelin handbook of inorganic and organometallic chemistry. 8th Edition. 132-140.

Avgouropoulos G, Manzoli M, Boccuzzi F, Tabakova T, Papavasiliou J, Ioannides T and Idakiev V. 2008. Catalytic performance and characterization of Au/doped-ceria catalysts for the preferential CO oxidation reaction. *J Catal*. 256:237-247.

Büchel R, Strobel R, Krumeich F, Baikerb A and Pratsinis SE. 2009. Influence of Pt location on $Baco_3$ or Al_2O_3 during Nox storage reduction. *J Catal*. 261:201-207.

Castoldi L, Lietti L,Forzatti P, Morandi S, Ghiotti G and Vindigni F. 2010. The NOx storage-reduction on PtK/Al_2O_3 lean NOx trap catalyst. *J Catal*. 276:335.

Chen Z, Yang Q, Li H, Li X, Wang L and Tsang SC. 2010. Cr–MnOx mixed-oxide catalysts for selective catalytic reduction of Nox with NH_3 at low temperature. *J Catal*. 276:56.

Daniel C, Clarté M, Teh S, Thinon O, Provendier H, Van Veen A, Beccard B, Schuurman Y, and Mirodatos C. 2010. Spatially resolved catalysis in microstructured reactors by IR spectroscopy: CO oxidation over mono- and bifunctional Pt catalysts. *J Catal.* 272:55-64.

Derrouiche S and Bianchi D. 2006. Modifications of the elementary steps involved in the O_2-oxidation of the adsorbed CO species over Pt/Al_2O_3 by co-adsorbed NO species. *J Catal*. 242:172.

Cant NW, Chambers DC and Liu I. 2011. The reduction of 15N14NO by CO and by H_2 over Rh/Sio_2: A test of a mechanistic proposal. *J Catal*. 278:162.

Chupin C, Van Veen AC, Konduru M, Després J and Mirodatos C. 2006. Identity and location of active species for NO reduction by CH_4 over Co-ZSM-5. *J Catal*. 241:103.

Qu Z, Zhang X, Yu , Liu X and Fu Q. 2015. Role of the Al chemical environment in the formation of silver species and its CO oxidation activity. *J Catal*. 321:113-122.

Gavin Chua YP, Kasun Kalhara Gunasooriya GT, Saeys M and Seebauer E. 2014. Controlling the CO oxidation rate over Pt/TiO_2 catalysts by defect engineering of the TiO_2 support. *J Catal.* 311:306-313.

Figueroa S and Newton M. 2014. What drives spontaneous oscillations during CO oxidation using O_2 over supported Rh/Al_2O_3 catalysts?. *J Catal*. 312:69-77.

Gates B, and Guilar V. 2008. Kinetics of CO oxidation catalyzed by highly dispersed CeO_2-supported gold. *J Catal*. 260:351-357.

Hamilton N, Warringham R, Silverwood I, Kapitán J, Hecht L, Webb P, Tooze R, Wuzong W, Frost C, Parker S and Lennon D. 2014. The application of inelastic neutron scattering to investigate CO hydrogenation over an iron fischer-tropsch synthesis catalyst. *J Catal*. 314:221-231.

M. Haruta and Daté M. 2001. Advances in the catalysis of Au nanoparticles. *Appl Catal*. 222:427-437.

Lindholm A, Currier NW, Li J, Yezerets A and Olsson L. 2008. Detailed kinetic modeling of storage and reduction with hydrogen as the reducing agent and in the presence of CO_2 and H_2O over a Pt/Ba/Al catalyst. *J Catal*. 258: 273-288.

Iglesias E and Weiss B. 2010. Mechanism and site requirements for NO oxidation on Pd Catalysts. *J Catal*. 272:74-81.

Forzatti P, Lietti L, Nova I, Morandi S, Prinetto F and Ghiott G. 2010. Reaction pathway of the reduction by CO under dry conditions of NOx species stored onto $PtBa/Al_2O_3$ lean NOx trap catalysts. *J Catal.* 274:163-175.

Hao Y, Mihaylov M, Ivanova E, Hadjiivanov K, Knözinger H and Gates B. 2009. CO oxidation catalyzed by gold supported on MgO: Spectroscopic identification of carbonate-like species bonded to gold during catalyst deactivation. *J Catal*. 261:137-149.

Hongjuan W, Hao Y, Feng P and Xiaomei N. 2015. Pt nanoparticles interacting with graphitic nitrogen of N-doped carbon nanotubes: Effect of electronic properties on activity for aerobic oxidation of glycerol and electro-oxidation of CO. *J Catal*. 325:136-144.

Ingelsten H, Zhao D, Palmqvist A and Skoglundh M. 2005. Mechanistic study of the influence of surface acidity on lean NO_2 reduction by propane in HZSM-5. *J Catal*. 232:68-79.

Wachs IE, Kim T, Burrows A, and Kiely CJ. 2007. Molecular/electronic structure–surface acidity relationships of model-supported tungsten oxide catalysts. *J Catal*. 246:370-381.

Kohyama M, Tomoki A and Yasushi M. 2015. Low-temperature CO oxidation properties and TEM/STEM observation of $Au/\Gamma\text{-}Fe_2O_3$ catalysts. *J Catal*. 324:127-132.

Haruta M, Tsubota S, Kobayashi T, Kageyama H, Genet MJ and Delmon B. 1993. Low-temperature oxidation of CO over gold supported on Tio_2, $A\text{-}Fe_2O_3$, And CO_3O_4. *J Catal*. 144:175-192.

NIST standard reference database 69: NIST chemistry webbook.

Ozbek MO and Niemantsverdriet JW. 2014. Elementary reactions of CO and H_2 on C-terminated $X\text{-}Fe_5C20\ 0\ 1$ surfaces. *J Catal*. 317:158-166.

Wang Y, Ma X, Wu Y, Lu Y, Xu J and Zhu Y. 2011. Effect of compensated codoping on the photoelectrochemical properties of anatase TiO_2 photocatalyst. *J Phys Che.* 115 16963–16969.

Pérez J, Kondratenko E and Debbagh M. 2005. Transient studies on the mechanism of N_2O activation and reaction with CO and C_3H_8 over Fe-silicalite. *J Catal*. 233:442-452.

Rivallan M, Ricchiardi G, Bordiga S and Zecchina A. 2009. Adsorption and reactivity of nitrogen oxides NO_2, NO, N_2O on Fe–zeolites. *J Catal*. 264:104-116.

Rivera AP, Tanaka K and Hinsanaga T. 1993. Photocatalytic degradation of pollutant over Tio_2 in different crystal structures. *Appl Catal B: Environ*. 3:37-44.

Rodriguez J, Evans J, Feria L, Vidal A, Liu P and Nakamura K. 2013. CO_2 hydrogenation on Au/Tic, Cu/Tic, and Ni/Tic catalysts: Production of CO, methanol, and methane. *J Catal*. 307:162-169.

Wade LG. 2006. Organic chemistry. 6th Edition. 6:139-142.

Zou X, Qi S, Xu J, Suo Z, An L and Li F. 2010. Study on Au/Al_2O_3 catalysts for low-temperature CO oxidation in Situ FT-IR. *J Nat Chem*. 19:307-312.

Xianyong S, Mueller S, Shi H, Haller G, Sanchez-Sanchez M, Van Veen A and Lercher J. 2014. On the Impact of co-feeding aromatics and olefins for the methanol-to-olefins reaction on HZSM-5. *J Catal*. 314:21-31.

Wonyong C, Sang-Hyup L, Palanichamy M, Narayanan L, Jae Y, Jae S and Jonghun L. 2014. Synergic photocatalytic effects of nitrogen and niobium co-doping in TiO_2 for the redox conversion of aquatic pollutants under visible light. *J Catal*. 310:91-99.

Yasuo I, Tomonobu M, Takumi M, Mitsutaka O, Masakazu D and Masatake H. 2009. A kinetic study on the low temperature oxidation of CO over Ag-contaminated Au fine powder. *J Catal*. 62:280-286.

Young Y, Meijun L, Wolfgang MS and Weitz E. 2007. Low-temperature Nox reduction with ethanol over Ag/Y: A comparison with $Ag/\gamma\text{-}Al_2O_3$ and BaNa/Y. *J Catal*. 246:413-427.

Liu J, Z. Guo, D. Childers, N. Schweitzer, C. L. Marshall, R. F. Klie, J.T. Miller and R.J. Meyer. 2014. Selective adsorption of manganese onto rhodium for optimized $Mn/Rh/SiO_2$ alcohol synthesis catalysts. *J Catal.* 313:149.

Cheng D, Xu H and Fortunelli A. 2014. Tuning the catalytic activity of Au–Pd nanoalloys in CO oxidation via composition. *J Catal*. 314:47-55.

Zhang H, Dai B, Li W, Wang X, Zhang J, Zhu M and Gu J. 2014. Non-mercury catalytic acetylene hydrochlorination over spherical activated-carbon-supported Au–Coiii–Cuii catalysts. *J Catal*. 316:141-148.

Collins SE, Aguirre A, Chen X, Delgado J, Calvino JJ and Berna S. 2014. Reversible deactivation of a $Au/Ce0.62Zr0.38O_2$ catalyst in CO oxidation: A systematic study of CO_2-triggered carbonate inhibition. *J Catal.* 316:210-218.

Yang K, Liu J, Si R, Chen X, Dai W and Fu X. 2014. Comparative study of Au/Tio_2 and Au/Al_2O_3 for oxidizing CO in the presence of H_2 under visible light irradiation. *J Catal.* 317:229-239.

Widmann D, Hocking E and Behm RJ. 2014. On the origin of the selectivity in the preferential CO oxidation on Au/Tio_2 – nature of the active oxygen species for H_2 oxidation. *J Catal.* 317:272-276.

He J, An Z, Dai Y, Li B and Yu C. 2014. Enhanced heterogeneous asymmetric catalysis via the acid–base cooperation between achiral silanols of mesoporous supports and immobilized chiral amines. *J Catal.* 317:105-113.

Zhao Z, Li Z and Lin YS. 2009. Adsorption and diffusion of carbon dioxide on metal−organic framework MOF-5. *Chem Res*. 48:10015-10020.

Petoud S, An J, Shade CM, Chengelis-Czegan DA, and Rosi NL. 2011. Zinc-adeninate metal−organic framework for aqueous encapsulation and sensitization of near-infrared and visible emitting lanthanide cations. *J Am Chem Soc*. 133:1220-1223.

Hafizovic J, Bjørgen M, Olsbye U, Dietzel PDC, Bordiga S, Prestipino C, Lamberti C and Lillerud KP. 2007. The inconsistency in adsorption properties and powder xrd data of mof-5 is rationalized by framework interpenetration and the presence of organic and inorganic species in the nanocavities. *J Am Chem Soc*. 129 3612-3620.

Tsao CS, Yu MS, Chung TY, Wu HC, Yu Wang C, Chang KS and Chen HL. 2007. Characterization of pore structure in metal−organic framework by small-angle x-ray scattering. *J Am Chem Soc*. 129 15997-16004.

White KA, Chengelis DA, Gogick KA, Stehman J, Rosi NL, and Petoud S. 2009. Near-infrared luminescent lanthanide MOF barcodes. *J Am Chem Soc*. 131:18069-180671.

Liu Q, Gao J, Gu F, Lu X, Liu Y, Li H, Zhong Z, Liu B, Xu G and Su F. 2015. One-pot synthesis of ordered mesoporous Ni-V-Al catalysts for CO methanation. *J Catal*. 326:127-138.

Ning X, Yu H, Peng F and Wang H. 2017. Electron transfer dependent catalysis of pt on N-doped carbon nanotubes: Effects of synthesis method on metal-support interaction. *J Catal*. 348:100-109.

Lonergan WW, Wang T, Vlachos DG and Chen JG. 2011. Effect of oxide support surface area on hydrogenation activity: Pt/Ni bimetallic catalysts supported on low and high surface area Al_2O_3 and ZrO_2. *Applied Catal.* 408:87-95.

Munir D, Irfan MF and Usman MR. 2018. Hydrocracking of virgin and waste plastics: A detailed review. *Renew Sustain Energy Rev*. 90:490-515.

Gao P, Li S, Bu X, Dang S, Liu Z, Wang H, Zhong L, Qiu M, Yang C, Cai J, Wei W and Sun Nat Y. 2017. Direct conversion of CO_2 into liquid fuels with high selectivity over a bifunctional catalyst. *Chem*. 9:1019-1024.

Cheng K, Zohu W, Kang J, Wen W, Pan Y and Wang Y. 2018. Bifunctional catalysis for the conversion of synthesis gas to olefins and aromatics. *Chem*. 10:1107-1112.

Kasipandi S and Bae JW. 2019. Spatially confined cobalt nanoparticles on zirconium phosphate-modified KIT-6 for an enhanced stability of CO hydrogenation to hydrocarbons. *Fuel*. 239:547-558.

Chung SH, Stosic D, Chowdhury AD, Van Der Wal LI, Fu D, Zecevic J, Travert A, Houben K, Baldus M and Weckhuys BM. 2019. Multiscale mechanistic insights of shaped catalyst body formulations and their impact on catalytic properties. *ACS Catal*. 9: 4792-4803.

Oenema J, Hofmann JP, Hensen EJM, Zečević J and Jong KP. 2020. Assessment of the location of Pt nanoparticles in Pt/zeolite Y/γ-Al_2O_3 composite catalysts. *Chem Cat Chem.* 12:615-622.

Sautel M, Elmaleh H and Leveiller F. 2000. Comparison of specific surface areas of a micronized drug substance as determined by different technique. *Stud Surf Sci Catal*. 128:633-642.

Gao M, Zou K, Deng Y, Zhao Z, Li Y and Chen G. 2017. An unprecedented case: A low specific surface area anatase/N-doped carbon nanocomposite derived from a new single source precursor affords fast and stable lithium storage ACS. *Appl Mater Interfaces.* 34:28527-28536.